images (7). Rather than repoint the telescope several times in each orbit, we elected to retain the 889-nm pointing to maximize the number of images in each orbit. This constrained us to image only the southern half of Jupiter in PC sequences.
7. C. J. Burrows, Ed., *Wide Field and Planetary Camera 2 Instrument Handbook* (STScI publication, Baltimore, MD, May 1994).
8. For those impacts where we detected waves, we used the center of the wave to identify the latitude and longitude of the impact site. We also looked for a central impact (that is, we looked for ejecta and used the material's position to estimate the impact location) and then used a circle of 3 or 5 pixels to define a center in this region. In most cases, we examined "before," "after," and later images of the site to make sure we had the best location estimate. We inferred impact times from the difference between predicted and inferred longitudes.
9. H. Weaver *et al.*, *Science* **267**, 1282 (1995).
10. R. A. West *et al.*, *ibid.*, p. 1296.
11. K. S. Noll *et al.*, *ibid.*, p. 1307.
12. T. Martin and the Galileo PPR Team, personal communication.
13. R. Carlson and the Galileo NIMS Team, personal communication.
14. The refraction effect would be only 3 km if the limb were at the 10-mbar level. The reduction in height due to refraction is the bending angle of a ray passing tangentially through the atmosphere times the distance from the tangent point (the limb) to the impact point. This bending angle is $N(0)\,(2\pi R_J/H)^{1/2}$, where $N(0)$ is the atmospheric refractivity at the tangent point, R_J is the radius of Jupiter, and H is the scale height of the density distribution, assumed to be exponential (this formula is valid in the limit of a small bending angle and a small value for H/R_J). The refractivity of hydrogen is $1.4 \times 10^{-4}\ \rho/\rho(0)$, where ρ is the density and $\rho(0)$ is the density at standard conditions.
15. H. Weaver *et al.*, *Science* **263**, 787 (1994).
16. S. K. Atreya, *Atmospheres and Ionospheres of the Outer Planets and Their Satellites* (Springer-Verlag, New York, 1986).
17. V. I. Bronshten, *Physics of Meteoric Phenomena* (Reidel, Boston, 1983).
18. T. Herbst, D. P. Hamilton, H. Bohnhardt, J. L. Ortiz-Moreno, unpublished results.
19. C. Chapman and the Galileo SSI Team, personal communication.
20. M. Belton *et al.*, *Space Sci. Rev.* **60**, 413 (1992).
21. To find the plume heights, we first measured the x and y positions of the plume top and of the center of Jupiter (*22*). We then computed the distance from the plume top to the planet center and subtracted the distance from the planet center to the point on the limb below the impact. Finally, we added the vertical distance from the 100-mbar level of the impact site to the Earth line-of-sight for the longitude and time of the impact (for times, we used our estimates from Table 2). This rough calculation is good to within the errors of our ability to define the planet center and plume top.
22. We used programs originally developed for Voyager data reduction, which were subsequently modified for UNIX and IDL by C. Barnet.
23. J. Scotti *et al.*, poster presentation at the 26th Annual Division of Planetary Sciences Meeting, Washington, DC, 31 October–4 November 1994.
24. M.-M. MacLow and K. Zahnle, *Bull. Am. Astron. Soc.* **26**, 926 (1994).
25. We navigated all the images in a given HST orbit to determine an average planet center and used this average planet center to extract and remap the region around each impact site onto a 20° by 20° longitude-latitude map, with 20 pixels per degree (*22*). From this map, we estimated the circle's central longitude by averaging the circle's east and west extrema and estimated its latitude by averaging the north and south extrema.
26. The algorithm was developed by T. Dowling and C. Santori based on an outline from H. Goldstein, *Classical Mechanics* (Addison-Wesley, Reading, MA, ed. 2, 1980), pp.40–41.
27. For the inner ring, fixing the intercept at 586 km (that is, assuming the inner and outer rings started at the same time and radius) yielded a velocity of 189 ± 10 m s^{-1} (formal error), almost consistent with models suggesting a 3:1 ratio for the speeds of the two fastest modes (*28*) (*4*). Solving for both the slope and intercept implied a velocity of 353 ± 83 m s^{-1} with an intercept of −635 ± 613 km; in this model, the inner ring propagated almost as fast as the outer ring but began expansion roughly 30 min later. Finally, constraining the radius to 0 at time 0 implied a velocity of 268 ± 9 m s^{-1} (formal error). Because the correct physical interpretation of the inner wave is still unidentified, all of the above are plausible assumptions, and we simply state that the velocity of the inner ring is in the range of 180 to 350 m s^{-1}.
28. A. P. Ingersoll and H. Kanamori, unpublished results.
29. The radius of deformation, L_d, is a characteristic scale length in atmospheric dynamics and is defined as c/f, where c is the wave propagation velocity and f is the Coriolis parameter $2\Omega\sin\phi$, where Ω is the angular velocity of the planet and ϕ is the planetographic latitude.
30. A. P. Ingersoll *et al.*, *J. Geophys. Res.* **86**, 8733 (1981).
31. During the Voyager era, there were 13 ovals separated by about 25° longitude on average, with the maximum separation being 61°. If one assumed a missing oval, that implied a wave pattern with n = 14. The HST data show only seven ovals with longitudinal spacing ranging from 110° to 28°, with about 50° being most common. The eastward drift rate of the features has remained constant at about 0.6° per day.
32. T. E. Dowling and A. P. Ingersoll, *J. Atmos. Sci.* **46**, 3256 (1989); G. P. Williams and R. J. Wilson, *ibid.* **45**, 207 (1988); P. S. Marcus, *Nature* **331**, 693 (1988).
33. M.-M. MacLow and A. P. Ingersoll, *Icarus* **65**, 353 (1986).
34. J. Clarke *et al.*, *Science* **267**, 1302 (1995).
35. P. J. Gierasch, B. J. Conrath, J. A. Magalhães, *Icarus* **67**, 456 (1986).
36. J. A. Holtzman *et al.*, *Publ. Astron. Soc. Pac.*, in press.
37. P. W. Chodas and D. K. Yeomans, personal communication.
38. We gratefully acknowledge the staff and management at the Space Telescope Science Institute (STScI) for their fortitude during these unusually challenging observations; we note in particular the assistance of our Comet Science Team colleagues H. Weaver, M. McGrath, and K. Noll, and the heroic efforts of A. Storrs during planning and execution of the observations. We thank J. Trauger and members of the WFPC2 Team for the marvelous instrument, and we also thank our anonymous referees for insightful comments on the manuscript. H.B.H. thanks C. Barnet and L. Gesner for support with software acquisition and development. These observations were made with the NASA-ESA Hubble Space Telescope, with support provided through grant GO-5624.08-93A from STScI, which is operated by the Association of Universities for Research in Astronomy under NASA contract NAS5-26555.

Impact Debris Particles in Jupiter's Stratosphere

Robert A. West, Erich Karkoschka, A. James Friedson, Mark Seymour, Kevin H. Baines, Heidi B. Hammel

The aftermath of the impacts of periodic comet Shoemaker-Levy 9 on Jupiter was studied with the Wide Field Planetary Camera 2 on the Hubble Space Telescope. The impact debris particles may owe their dark brown color to organic material rich in sulfur and nitrogen. The total volume of aerosol 1 day after the last impact is equal to the volume of a sphere of radius 0.5 kilometer. In the optically thick core regions, the particle mean radius is between 0.15 and 0.3 micrometer, and the aerosol is spread over many scale heights, from approximately 1 millibar to 200 millibars of pressure or more. Particle coagulation can account for the evolution of particle radius and total optical depth during the month following the impacts.

Aerosol debris from the impacts of fragments of comet Shoemaker-Levy 9 can serve as a tracer to study the jovian stratospheric circulation, which has been inferred only indirectly from measurements of thermal contrast and solar radiative heating (*1*). Analogous studies of particles injected into the terrestrial stratosphere by volcanic eruptions have provided a wealth of data about the earth's atmosphere (*2*).

Aerosol debris particles are valuable tracers of the stratospheric wind field because their global distribution can be determined with high spatial resolution from a few images. We obtained images taken with the Wide Field Planetary Camera 2 (WFPC2) on the Hubble Space Telescope (HST). To learn as much as possible about the altitudes of the particles and about particle microphysical processes, especially the particle size that determines the loss rate from sedimentation, we imaged Jupiter at a variety of wavelengths (from 230 to 955 nm), and we scheduled exposures to provide coverage of emission angle as features rotated across the disk. The opacity provided by molecular scattering at ultraviolet (UV) wavelengths and by CH_4

R. A. West, K. H. Baines, and A. J. Friedson are with the Earth and Space Sciences Division, Jet Propulsion Laboratory, California Institute of Technology, Pasadena, CA 91109, USA. E. Karkoschka is with the Lunar and Planetary Laboratory, University of Arizona, Tucson, AZ 85721, USA. M. Seymour is with University College, London, UK, and the Earth and Space Sciences Division, Jet Propulsion Laboratory, California Institute of Technology, Pasadena, CA 91109, USA. H. B. Hammel is with the Department of Earth Atmosphere and Planetary Sciences, Massachusetts Institute of Technology, Cambridge, MA 02139, USA.

opacity in the 893-nm CH_4 filter, as well as emission angle coverage in these filters, provided channels for vertical sounding. The broad wavelength coverage provided sensitivity to particle size if the particle radii were less than about 0.5 μm. Our photometric measurements (3) were also sensitive to the imaginary part of the particle refractive index that provided a constraint on composition.

Observations and Data Reduction

Our program and that of Hammel *et al.* (4) made use of the same WFPC2 images taken between 15 July and 24 August 1994. Images were obtained before, during, and after the week of the impacts. The WF images have a resolution of 770 km per line pair, and the PC images have a resolution of 342 km per line pair at the subspacecraft point. We derived optical depths of particles for all the F255W and CH_4 filter images taken on 23 July, 30 July, and 24 August, and for a small number of images taken close to the time of impact. The important parameters for this study were the effective wavelength (the wavelength obtained by weighting the spectral transmission of the instrument sensitivity with the solar flux) and the effective depth of penetration of photons (the pressure level where unit optical depth is reached for vertical viewing in the absence of aerosols). These can be found in Table 1, along with the low-temperature CH_4 absorption coefficients and effective geometric albedos used to establish an absolute calibration.

We determined absolute calibration factors for the images by requiring that the geometric albedo (here we mean the ratio of the flux from Jupiter at a phase angle of 10.5° to that from a Lambert-reflecting disk of equal projected area facing the sun) agree with published measurements (5, 6). Some of the images show Galilean satellites. Because the albedo of the satellites is essentially the same at wavelengths of 893 and 953 nm (6), the relative intensity calibration between both filters can be checked. Calibration factors derived from satellite images implied that Jupiter's albedo at a wavelength of 893 nm increased by 10% from July 1993 to July 1994. We consider this to be possible because previous temporal variations in excess of 20% have been observed at some latitudes, although Moreno *et al.* (7) found no change over the same period.

After processing the images, we began to construct photometric models to compare with the data. We found an asymmetry between east and west for the two longest-wavelength filters. Previous studies found no such asymmetry, and we suspect that the flat field images contained a spurious gradient. To remove the gradient, we applied a linear ramp across the image such that a net difference (the difference between the east limb and west limb at the equator) of 12% for the F953N filter and 24% for the CH_4 filter nullified the apparent asymmetry. An asymmetry might also be caused by an error in image centering, but after checking the navigation and comparing the location of features in different filters, we considered this to be implausible.

Table 1. Spectral characteristics of the filters used in this study. Filter passbands and exposure times are listed in (4). λ_E is the effective wavelength when convolved with the solar spectrum, A is Jupiter's geometric albedo when convolved with the camera sensitivity (5, 6), K is the effective CH_4 absorption coefficient [sensitivity convolved with the low-temperature CH_4 absorption coefficients (6)], and P_0 is the pressure level where unit optical depth is reached for vertical viewing in the absence of aerosols. Blank spaces indicate wavelengths where the reflected intensity is determined by the optical properties of the cloud particles in the pressure range 10 mbar to 5 bar.

Filter	λ_E (nm)	A	K (km-amagat)$^{-1}$	P_0 (bar)
F218W	230	0.31	0.0	0.18
F255W	275	0.28	0.0	0.35
F336W	335	0.29	0.0	1.2
F410M	410	0.36	0.0	2.7
F547M	550	0.50	0.02	
F555W	555	0.49	0.2	
FQCH4	893	0.049	25.0	0.38
F953N	955	0.43	0.3	

Particle Optical Depth, Mean Radius, Refractive Index, and Distribution

The impact regions show dark features in images taken with all the filters except CH_4. At visible wavelengths (Fig. 1), the material appears dark and slightly brown because of greater absorption of light at short wavelengths. This idea is borne out by quantitative analysis. Figure 2 shows I/F (I is intensity and πF is the incident solar flux) as a function of longitude for a cut through the dark core region of impact sites D and G. The UV contrast features are broader than those seen at the other wavelengths both because of rotational smear during the 300-s exposure and because of the greater absorption cross-section in the UV.

Fig. 1. The D and G impact sites imaged with the WFPC2 almost 2 hours after the G impact on 18 July 1994. The diameter of the main wave (circular ring) is about 7000 km.

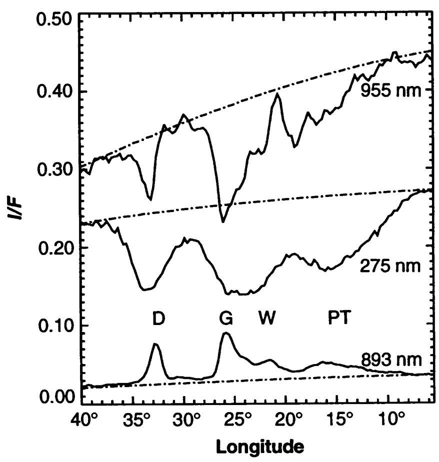

Fig. 2. I/F (I is intensity and πF is the incident solar flux) is shown for three wavelengths for a cut across the D and G impact sites along a latitude line, close in time to the image shown in Fig. 1. The letter W shows the location of a wave feature, and PT corresponds to the location of a crescent-shaped dark (except through the CH_4 filter) region that we take to be the plume terminus (where the outlying ejected plume material came to rest). The dot-dash lines are projected values for the undisturbed atmosphere. They were derived by fitting I/F to a generalized Minnaert law: $\ln(\mu I/F) = C_0 + C_1x + C_2x^2 + C_3x^3$, where μ is the cosine of the emission angle, $x = \ln(\mu\mu_0)$, μ_0 is the cosine of the solar incidence angle, and the coefficients are found by a least-squares fit to intensities in the undisturbed regions.

Determination of particle optical and physical properties requires radiative transfer models of the atmosphere that accurately account for multiple scattering and absorption by aerosols and gas. We first examined the darkest pixel (at continuum wavelengths) for the A and E sites on 17 July and for the A, C, F, and H sites on 21 July. The darkest pixel for those dates has I/F values similar to those of the darkest pixels shown in Fig. 2. At small spatial scales, the contrast is diminished relative to what a perfect imaging system would provide. We have not corrected for this effect, and we do not know the magnitude of the error it produces in our results.

We modeled data for filters F255W, F336W, CH_4, and F953N. For all points, we used at least two emission angles to determine the limb darkening. The optical thickness of the debris haze was great enough [2 to 5 in the infrared (IR)] that a crude model (a single semi-infinite layer) could be used for the underlying atmosphere. The CH_4-band limb darkening in connection with the 953-nm continuum reflectivity agreed with the data if the debris material was near the 100-mbar pressure level. If the upper boundary was at a pressure of 1 mbar or less, the lower boundary had to be pushed down to about 200 mbar. Again, the average pressure level is near 100 mbar. If the average pressure were much less, the planet would be quite bright at the limb in the CH_4 filter, which was not observed.

Models of reflectivity at 275 nm (with the F255W filter) require UV-absorbing material to be at pressures less than a few millibars in order to account for the dark limb. Some of the absorption is due to S_2, especially during the first few days following the impact, so the total optical depth we report is the sum of aerosol and gas components. The S_2 contribution is probably small, judging by the figure in (*8*), but a more thorough analysis needs to be done. By combining the UV and CH_4 data, we found that the material in the fresh, dense core regions we examined must extend over many scale heights, from a few millibars or higher altitude to the 200-mbar level or deeper. The deep aerosol population also accounts for the observation (*4*) that the zonal wind shear determined by tracking the particles in the dense regions is the same as the tropospheric wind shear at the cloud top deduced from Voyager images and the present data set. The aerosols at a few millibars or higher altitude are consistent with the visibility of bright debris features in the strong CH_4 bands in the 1600- to 3200-nm spectral region (*9*).

The contrast at continuum wavelengths requires that the particles be more absorbing than most of the material in the ambient jovian atmosphere. As part of the modeling effort, we found that the imaginary part of the refractive index was 0.006 from the near-infrared to blue, then increased to 0.012 in the F336W filter and further increased to 0.02 in the F255W filter. We also successfully modeled the reflectivity with imaginary refractive indices that are twice as large at long wavelengths. Figure 3 summarizes these results and compares the derived refractive indices with some candidate materials. The reflected intensities are insensitive to the real part of the refractive index, and our models assumed values of 1.4 and 1.44 for different cases.

Refractive indices derived above for the dark core regions are equally valid for particles in the outer diffuse regions and in the transient wave features. The fact that the wave is bright when seen through the CH_4 filter means that particles are present at altitudes higher than those of most of the particles in Jupiter's undisturbed atmosphere. In the undisturbed regions, most of the light reflected in the CH_4 band comes from scattering in the ammonia cloud region between 600 mbar and 250 mbar (the temperature minimum and tropopause are at the 100-mbar level).

The fact that both the transient and more permanent debris particles have the same optical properties suggests that both types of particles come from a parent gas that exists mainly in the high stratosphere where temperatures are too warm for condensation to occur except during the expansive phase of a passing wave. The more permanent debris could be material that came to rest at a lower altitude (where the temperature is sufficiently low to induce condensation), either by turbulent mixing of entrained gas as the fireball rose (the dark core regions) or as material that penetrated to some threshold depth on final impact of the rebounding plume (the outlying regions). A candidate is CS_2, which was observed spectroscopically (*8*). It would condense in the ambient atmosphere at pressures in the range from 8 to 63 mbar if its mixing ratio were in the range from 10^{-3} to 10^{-7}. However, its imaginary refractive index is too small to account for the contrast at most wavelengths (*10*).

Water, ammonia, and carbon dioxide ice that might be present from an impacting body or be of jovian tropospheric origin have imaginary refractive indices (*11*) that are far too small to account for the absorption over the entire spectral range of our observations. Even S is not sufficiently absorbing over most of the spectrum, by orders of magnitude in the red (*12*). Candidates that offer more promise are graphite, dirty silicate, and some organics. We show in Fig. 3 the imaginary refractive indices of "astronomical graphite" and "astronomical silicate," which were proposed (*13*) as candidates for interstellar grains. The astronomical graphite and silicate, which might be expected to be produced in an expanding fireball environment, have refractive indices whose flat shape from the blue to near-IR agrees with the shape inferred from our analysis for the debris particles, but these candidates produce spectra that are too flat between 275 and 410 nm.

Polymerized hydrogen cyanide [poly-HCN; see (*14*)] is an interesting candidate whose imaginary refractive index has a spectral dependence similar to the derived shape for the debris particles. The poly-HCN material shown in Fig. 3 is very rich in N. Complex organics rich in S and N may also qualify as candidates whose vapor pressure to mixing ratio relation is in the range needed to have both gas and condensed phases present near the 1-mbar level, to account for the visibility of the waves. HCN was observed in spectra obtained by the James Clerk Maxwell Telescope (*15*), and HCN is relatively abundant as an end product in some chemical models of the evolving fireball (*16*). Organic material rich in S and N, even in trace amounts, is therefore an attractive candidate for the agent responsible for the dark brown color.

Most of the UV spectral features (*8*) are produced by gases (S_2, CS_2, NH_3, and H_2S), which could have come from either the impacting bodies or the jovian atmo-

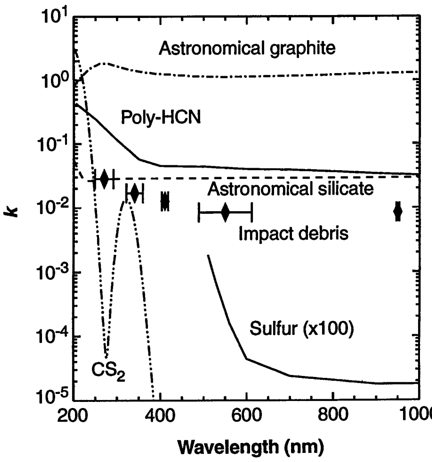

Fig. 3. The imaginary part of the refractive index (*k*) is shown as a function of wavelength for several candidate aerosol materials as well as the range of values inferred for the debris. The laboratory measurements are from (*10–14*). The horizontal location and size of the symbols indicate the filter wavelengths and the size of the passband. The vertical size indicates the range of values that were able to fit the observations.

sphere, provided that the impacting body penetrated into or below the hypothesized NH_4SH cloud whose base is near the 2-bar pressure level. The gases mentioned above are abundant products of experimentally shocked carbonaceous chondrite material (*17*). Refractory particles (silicates and metals) would also be present in abundance if most of the debris material came from the impacting body (*18*). Some of these were observed in atomic form in UV spectra (*8*) as ions and neutrals that reside in the thermosphere and ionosphere of Jupiter. But refractory particles cannot account for much of the observed particulate opacity if a single material is responsible for both the transient and more permanent aerosol debris as the color and contrast suggest. In that case, a jovian origin for the bulk of the particulate debris is indicated.

Any attempt to relate observed color to composition is complicated by the fact that only a trace amount of strongly absorbing material is needed to darken bright material. Furthermore, reports of H_2O, silicate, and S features in IR (*19*) and UV spectra (*8*) lead to the expectation that the condensed phases of these constituents would be abundant in the atmosphere, and their origins, chemical evolutions, and final destinations in a fireball plume are probably diverse. It is therefore puzzling that the material is homogeneous in terms of its color.

The initial modeling effort yielded optical depths in the core regions that were between 2 and 5 at 893 nm and were several times larger at 275 nm. The ratio of optical depth at the two wavelengths is consistent with the ratio for spherical particles whose mean radius is in the range from 0.15 to 0.3 μm. The models are not sensitive to the variance or form of the size distribution, provided the variance is not large. A model in which aerosols with a radius of 0.25 μm mix uniformly with the gas between 1 mbar and 200 mbar can quantitatively account for the reflectivity in the strong CH_4 and H_2 absorption bands between 1600 and 3200 nm (*9*), and this is the type of model we used for the next phase of the study.

We derived particle optical depth at 275 and 893 nm for all longitudes imaged on 23 July (1 day after the last impact), 30 July, and 24 August. We had full longitudinal coverage on 23 July, but there was a gap between longitudes 120 and 140 in the UV on 30 July, whereas some longitudes on 30 July and 24 August were observed only at a high emission angle. The goals of these studies were to assess the global aerosol debris inventory and to track its evolution during the month following the impacts. An accurate assessment of the inventory requires an accurate derivation of optical depth even for regions of low optical depth. This effort made use of more sophisticated aerosol models to carefully account for the optical properties of the preimpact stratospheric haze and the tropospheric particle phase function and single scattering albedo as functions of wavelength and latitude. Once these were modeled properly in the latitude region −36.5° to −56.2° (all latitudes are planetocentric and all longitudes are System III), which bounds 80% or more of the debris, we added haze particles of radius 0.25 μm and solved for the best-fit optical depth as a function of latitude and longitude.

Three models for the vertical distribution of the haze were used. They all have debris particles up to altitudes where the pressure is 0.3 mbar, and the particles are mixed with the gas scale height down to some higher pressure. To determine if the aerosols extend as deep as 200 mbar in the diffuse regions as well as in the dark core regions, we examined the limb darkening

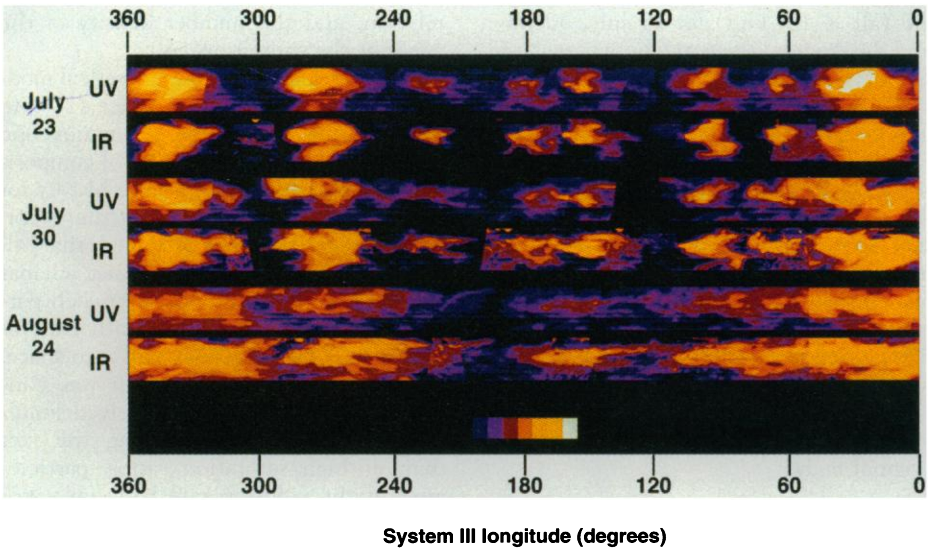

Fig. 4. Optical depths of debris material are shown for wavelengths of 275 and 893 nm as functions of latitude (between −36.5° and −54.2°) and longitude for 23 July, 30 July, and 24 August. Each strip has latitude −36.5° at the top and latitude −54.2° at the bottom. The color steps at the bottom calibrate the colors in terms of the optical depth. White corresponds to optical depth 12.0 or higher in the UV. Moving to the left in the color scheme, the values are 4.0, 2.0, 1.0, 0.5, 0.2, and 0.1. Those values should be divided by 4 to obtain optical depths in the 893-nm images.

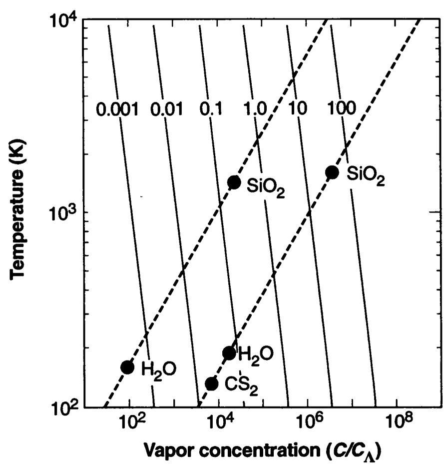

Fig. 5. The mean particle radius that would condense out of an exponentially expanding fireball parcel cooling along an adiabat, plotted as a function of temperature and vapor concentration. Concentration C is normalized to $C_\Lambda = [\alpha v(3\Omega/4\pi)^{2/3}\tau_s]^{-1}$, where α is the sticking coefficient, v is the vapor thermal velocity, Ω is the molecular volume in the condensed phase, and τ_s is the saturation ratio time scale. Thin solid lines are contours of grain radius in units of micrometers. Thick dashed lines represent two possible adiabats that might be characteristic of the thermal trajectories followed by parcels in a fireball. Solid circles are marked on the two adiabats at the temperature and vapor concentration at which each substance would condense in a parcel following the adiabat. The position of the solid circles indicates the mean grain radius expected for the vapor indicated and for the corresponding adiabat. The two adiabats correspond to cases where the vapor concentration is 1.2×10^{14} and 1.5×10^{16} cm^{-3} when the temperature is 2500 K. (For reference, a concentration of 10^{15} cm^{-3} of water vapor corresponds to a total mass of 1.2×10^{14} g spread uniformly through a sphere of radius 100 km. For "silicate" or CS_2 vapor, the mass would be greater by a factor of 3 to 4.) Where the adiabats fall on the plot depends on the value of C_Λ, which in turn is most sensitive to the value used for τ_s. Here we have used $\tau_s \simeq 10$ s, corresponding to a thermal cooling time of ~250 s, and we chose $\alpha = 1$.

in models with aerosol layers reaching the 10-, 80-, and 200-mbar pressure levels. Preliminary results in the near-IR do not favor one model over another. There is considerable scatter in the UV results as well, but the majority of locations at intermediate optical depth ($\tau \sim 1$) are best fit by the model with aerosols between 0.3 and 10 mbar. Our data are insensitive to the altitude of the top of the aerosol layer, provided it is at a pressure of less than a few millibars. Although the mean optical depth in the UV is several times higher than the mean optical depth in the near-IR, there is also considerable scatter in that ratio. We did not take into account tropospheric cloud height variations as a function of longitude, and perhaps most of the scatter in the 893-nm band is due to such variations.

The distribution of debris haze between latitudes $-36.5°$ and $-54.2°$ for the three dates is shown in Fig. 4 for the model with the haze between 0.3 and 80 mbar. The model with particles mixed down to 200 mbar produces a similar pattern, but the optical depths are higher for that case. The ratio of optical depth for the model with aerosols extending to 200 mbar to that for the model with aerosols extending to 10 mbar is a factor of 2 in the optically thick regions and is much higher in optically thin regions.

On 23 July the debris was close to the impact locations, although zonal wind shear and eddy motions had redistributed debris from the early impacts (*4*). The largest optical depths are greater than 15 (the maximum value we tested) in the UV and greater than 3 in the near-IR. The greatest optical depths correspond to impact sites L (near longitude 340°) and K-W (280°) and the D, G, R, and S regions (longitudes 5° to 50°). The UV optical depth dropped significantly by 24 August, whereas at 893 nm it increased. During the same interval, the debris pattern was dispersed in the east-west direction by zonal wind shear. When integrated over 360 degrees of longitude and 17.7 degrees of latitude (6.48×10^9 km^2) the optical depths at 275 nm are 7.0, 4.6, and 3.0 (all $\times 10^9$ km^2) for 23 July, 30 July, and 24 August, respectively, whereas the numbers (same units) at 893 nm are 1.1, 1.5, and 1.5. We will return to this observation in the context of aerosol microphysical models described in the next section. The ratio of optical depths at the two wavelengths can be understood if the particle mean radii are 0.21, 0.24, and 0.28 μm on the three dates. The total volume of debris particles on the three dates would equal the volume of a sphere with radius 0.51, 0.52, and 0.45 km. If these particles were part of the impacting bodies and not jovian atmospheric material, their derived volume sets a lower limit on the size of the original body.

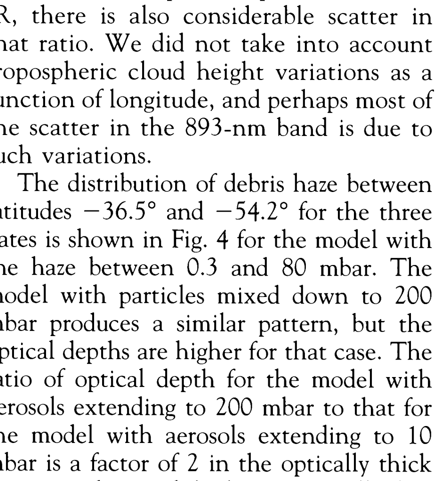

Fig. 6. Time scales relevant for physical processes occurring in the jovian troposphere and stratosphere. Solid curves indicate sedimentation times for particles of the indicated radius. Dashed curves indicate coagulation times for an initial population of 0.1 and 0.5 μm particles. The initial particle number density for the two cases was taken to be 570 and 23 cm^{-3}, respectively. The dotted curve indicates the eddy diffusive time scale for the jovian troposphere-stratosphere (*24*).

Aerosol Microphysical Models

We do not know the composition of the aerosol nor the thermal histories of parcels that carried the condensible vapor, which for a given composition influenced the eventual size and number of particles. It is nevertheless useful to discuss one likely scenario for the production of aerosol, because it will serve to illustrate how observed properties of the aerosol may eventually be linked to the microphysical and gas dynamical processes that led to its formation.

Aerosol formation in a plume. Scattered sunlight seen on the limb of the planet shows that particles reached very high altitudes (>3000 km) (*4*). The vapor that eventually condensed into these aerosols most likely had its origin in the superheated gas of a rising fireball. This idea is supported by the shape and growth of the plumes with time, which suggest that the particles were on ballistic trajectories with velocities comparable to that expected for the vertical rise of a fireball. As each fireball rose, it cooled by virtue of its volume expansion and by radiative cooling, and eventually its temperature dipped below the saturation point for a condensible vapor. Further cooling may have led to the condensation of a sequence of increasingly more volatile vapors.

The particles would not form at the instant the vapor was cooled below its saturation point. Significant nucleation (the formation of condensation nuclei large enough to be thermodynamically stable) requires supersaturation of the vapor to a critical value that depends on the type of nucleation process (that is, homogeneous, ion-induced, or heterogeneous nucleation). After the critical supersaturation is achieved, condensational growth on the stable nuclei may proceed rapidly until the available vapor is depleted. The final number density and size of the grains depend primarily on the cooling rate of the gas, the temperature-vapor pressure relation, and the number density of the vapor at the saturation point.

We developed a simple numerical model, based on work by Lattimer (*20*), to estimate the mean particle radius and number density given an aerosol composition and a density-temperature history for the fireball parcels containing the vapor. For simplicity, it was assumed that all fireball parcels followed a moist adiabat and that the specific volume of each parcel increased exponentially with time as the fireball expanded outward into space. Only homogeneous nucleation was considered. Two equations were solved simultaneously, the first expressing the fact that, at high saturation ratios, particles grow at the collision rate between vapor molecules and grains, and the second describing the depletion of vapor by nucleation and condensational growth (*21*). To a good approximation, the final mean particle radius $\bar{r}$ is found to be proportional to the parameter $\Lambda = \tau_s/\tau_c$, where τ_s is the e-folding time (time required to change by the Λ factor e) for the increase in the saturation ratio at the time the vapor first becomes saturated and is directly proportional to the cooling time scale (*22*), and τ_c is the collision mean free time between vapor molecules at saturation. Λ is a measure of the number of collisions occurring in a time τ_s. For $\Lambda \gg 1$, $\bar{r} \simeq \xi(\Lambda/3)(3\Omega/4\pi)^{1/3}$, where Ω is the effective volume of a molecule in the condensed phase and $\xi \simeq 0.05 - 0.3$ is a multiplicative factor found from the numerical solution. Once $\bar{r}$ has been estimated, the final total particle number can be determined from conservation of mass of the condensible species and the assumption of complete condensation of the available vapor.

Figure 5 illustrates the final grain radius expected for three aerosol compositions and for two adiabats. In a compact, relatively dense fireball, refractory materials such as silicates would form particles larger than 10 μm in radius, whereas materials as volatile as water would form grains smaller than 0.1 μm. In a less dense fireball, production of smaller grains is favored for each substance. If the thermodynamic histories of fireball parcels, determined either through analysis of the observations or through numerical simulations, can be plotted on Fig. 5, then it should be possible to estimate the radii of the particles that would have condensed in the plume for a given or conjectured aerosol composition and to compare this estimate with any grain sizes inferred from observations of plumes on the limb.

Aerosol evolution in the atmosphere. Aerosols injected or condensed in the atmosphere may have evolved further through coagulation and sedimentation and, if at all volatile, evaporation. Particles reentering the stratosphere from the high-altitude plumes may have ablated and possibly recondensed to form a different size distribution than they had in the plume. Because of these processes, one must be careful not to assume that the properties of the aerosols measured in the dark spots are characteristic also of the population of grains in the plumes.

Figure 6 shows the time scales for sedimentation and coagulation. The sedimentation time is the time required for a particle of given size and a density of 2 g cm^{-3} to fall one scale height, moving at its terminal velocity (*23*). Particles with radii ~0.5 μm and smaller would remain suspended above the 100-mbar level for more than 3 months, whereas grains larger than a few microns in radius would sediment into the troposphere within a few days. The coagulation time is the e-folding time required to reduce the concentration of particles of a given size by coagulation with other particles to form larger grains. As a given mass of aerosol is converted into larger grains, the particle concentration is reduced and the coagulation time increases. In Fig. 6, we show coagulation times for particle sizes $\bar{r}$ of 0.1 and 0.5 μm, using a number density n of grains chosen to reproduce the observed optical depth in the core of the dark spots; that is, $n \simeq \tau/(Q\pi\bar{r}^2 D)$, where $\tau \sim 5$ is the optical depth and $Q \sim 2$ is the extinction efficiency of the grains at a wavelength of 275 nm, and $D \sim 100$ km is the depth of the dust cloud. At these densities, particles 0.1 μm and less in radius would be expected to coagulate to form larger particles in a matter of a few days, but more than a month is required for coagulation to produce grains larger than 0.5 μm. Hence, if the aerosol in the dark spots were initially injected in the form of a relatively high density (>500 cm^{-3}) of grains smaller than 0.1 μm in radius, then coagulation would ensure that the dominant grain radius during the period between a few days and a month after the impacts was in the range 0.1 to 0.5 μm.

Although there is some loss of particle volume between 30 July and 24 August, most of the temporal behavior seen cannot be explained by loss from sedimentation. Larger particles fall faster than smaller ones, and sedimentation would cause optical depth to decrease with time at both wavelengths, but more rapidly in the IR, which is contrary to what is seen. Temporal changes in integrated optical depth during the period from 23 July to 24 August can be explained chiefly by coagulational growth of the particles. The UV optical depth falls because the decrease in particle column density implied by their growth outweighs any change in the extinction cross-section. For the IR optical depth, the change in extinction cross-section is the more important effect because it increases so rapidly with particle size at IR wavelengths. The IR optical depth increases with time because of this behavior. On the basis of our model of the particle microphysics, we expect debris particles to be present in the jovian stratosphere for a substantial portion of a year after the impacts. Future observations of their latitudinal distribution will fulfill our original goal of learning more about the stratospheric meridional circulation.

REFERENCES AND NOTES

1. B. J. Conrath, P. J. Gierasch, S. S. Leroy, *Icarus* **83**, 255 (1990); R. A. West, A. J. Friedson, J. F. Appleby, *ibid.* **100**, 245 (1992).
2. C.R. Trepte and M. H. Hitchman, *Nature* **335**, 626 (1992).
3. When convolved with the solar spectrum, the F218W filter transmits 3% of its total from wavelengths longer than its nominal passband. The data were processed for bias and dark-count subtraction, and divided by flat field frames by members of the science support staff at the Space Telescope Science Institute (STSI). These procedures yielded images whose relative (pixel-to-pixel) calibration was accurate to a few percent or better, depending on the filter (two exceptions are discussed elsewhere). The calibrated images suffer from a wavelength-dependent distortion produced chiefly by the field corrector. We used computer programs developed by the WFPC2 science team at the Jet Propulsion Laboratory to map the images onto a nondistorted and uniform projection. We then applied a calibration factor to establish the absolute intensities.
4. H. B. Hammel *et al.*, *Science* **267**, 1288 (1995).
5. L. Wallace, J. J. Caldwell, K.-H. Fricke, *Astrophys. J.* **172**, 755 (1986).
6. E. Karkoschka, *Icarus* **111**, 174 (1994). For wavelengths longer than 300 nm we used the full-disk albedo of Jupiter in July 1993 when Jupiter's phase angle was similar (within 1 degree) to its value during July to August 1994. For filters F218W and F255W, Jupiter's full-disk albedo spectrum was taken from Orbiting Astronomical Observatory (OAO) data (*5*) and increased by 6%, because the OAO team assumed solar U magnitude (the brightness in the standard U filter) was −25.95, whereas the current value is −25.89. With this adjustment, both spectra are almost identical in the overlapping spectral region. Jupiter's albedo for each filter was determined by multiplying the HST filter and instrument transmission curves with the solar spectrum and convolving this with Jupiter's spectrum.
7. F. Moreno *et al.*, *Geophys. Res. Lett.*, in press.
8. K. Noll *et al.*, *Science* **267**, 1307 (1995).
9. G. Orton *et al.*, *Science* **267**, 1277 (1995); K. H. Baines *et al.*, paper presented at the 26th Annual Meeting of the American Astronomical Society, Division for Planetary Sciences, Bethesda, MD, 31 October 1994.
10. R. L. Gustavsen, thesis, Washington State University (1989).
11. J. V. Martonchik, G. S. Orton, J. F. Appleby, *Appl. Opt.* **23**, 541 (1984); S. G. Warren, *ibid.*, p. 1206; *ibid.* **25**, 2650 (1986).
12. R. Sasson, R. Wright, E. T. Arakawa, C. Sagan, B. N. Khare, *Icarus* **64**, 368 (1985).
13. B. T. Draine, *Astrophys. J. Suppl. Ser.* **57**, 587 (1985).
14. B. N. Khare *et al.*, *Can. J. Chem.* **72**, 678 (1994).
15. T. Owen *et al.*, paper presented at the 26th Annual Meeting of the American Astronomical Society, Division for Planetary Sciences, Bethesda, MD, 31 October 1994.
16. K. Zahnle, personal communication.
17. T. N. Tingle, J. A. Tyburczy, T. J. Ahrens, C. H. Becker, *Origins Life Evol. Biosphere* **21**, 385 (1992).
18. G. B. Field, G. P. Tozzi, R. M. Stanga, *Astron. Astrophys. Lett.*, in press.
19. G. L. Bjoraker, T. Herter, G. Gull, S. Stolovy, B. Pirger, paper presented at the 26th Annual Meeting of the American Astronomical Society, Division for Planetary Sciences, Bethesda, MD, 31 October 1994; P. D. Nicholson, *et al.*, in preparation.
20. J. M. Lattimer, in *Proceedings of the Conference on the Formation of Planetary Systems*, CNES International Summer School, Grasse, France, 1 to 27 August 1980, A. Brahic, Ed. (CNES, Cepadues, France, 1982), pp. 190–282.
21. Additional assumptions were made in the derivation of the equations: The saturation ratio was assumed to be large compared with unity at the time of peak nucleation rate, and the size of the condensation nuclei was neglected in comparison with the final grain size. The results were found to be consistent with these assumptions. Moreover, the probability of a vapor molecule sticking to a grain when colliding with it was taken to be unity [H. R. Pruppacher and J. D. Klett, in *Microphysics of Clouds and Precipitation*, (D. Reidel, Dordrecht, Holland, 1978), pp. 358–411].
22. The saturation time scale is related to the thermal cooling time τ_T by $\tau_s = \tau_T\,(b/T_c - 1)^{-1}$, where T_c is the condensation temperature of the material and its equilibrium vapor pressure is given in dynes cm^{-2} in the general form $p_v = \exp(a - b/T)$.
23. For all but the largest grains, the drag on the particles falls in the "molecular regime" of behavior, which applies when the grain radius is much less than the mean free path of the air molecules.
24. B. Landry, M. Allen, Y. L. Yung, *Icarus* **89**, 377 (1991).

25. Many people contributed to this work. We are especially grateful to J. Trauger and members of the WFPC2 team, who supplied software and effort to remove image distortion; and to J. Clarke, who supplied detailed sensitivity profiles for the UV filters. The scheduling and science support teams (especially, A. Storrs) at the STSI went to extraordinary efforts to provide timely data reduction and made resources at the institute available. We thank J. Mills of MIT and A. Simon at New Mexico State University for their help with data reduction. E. De Jong produced Fig. 1, with assistance from P. Andres, M. McAuley, and J. Hall. We benefited greatly from discussions with B. Fegley, C. Sagan, K. Zahnle, and members of the HST observing campaign who shared their data and ideas, especially S. Atreya, R. Beebe, J. Clarke, A. Ingersoll, K. Noll, M. McGrath, H. Weaver, and R. Yelle. We thank R. Gustavsen of Los Alamos National Laboratory for supplying optical constants for CS_2. This work was done by the Jet Propulsion Laboratory, California Institute of Technology, under contract with the STSI and NASA. Support was provided by NASA through grant number FY 459-20-12-08-49 from the STSI, which is operated by the Association of Universities for Research in Astronomy under NASA contract NAS5-26555.